Vol.9, Issue No 3, Sep 2019

Parallel homogenization analysis of FW-CFRP for high-pressure hydrogen tanks considering fiber waviness

Poornima.K,Sharanappa Koni,Sridhar Gowda
Asst. Prof, Asst. Prof, Asst. Prof
mechpoornima@gmail.com, sharanukoni@gmail.com, sridharmpheroor@gmail.com
Department of Mechanical, Proudhadevaraya Institute of Technology, Abheraj Baldota Rd, Indiranagar, Hosapete, Karnataka-583225

Abstract
This work built a simulator for high-pressure hydrogen storage containers made of carbon-fiber-reinforced plastics (CFRPs) using the filament winding (FW) technique. The simulator accommodates for macro-, meso-, and micro-scale structures. An in-depth examination that takes FW-CFRP fibre bundle tape imperfections into consideration is now possible thanks to the created simulator. We created a parallel computing system for three-scale homogenisation using the domain decomposition approach since numerical simulations taken into account fibre imperfections increase memory utilisation and processing time. By running numerical examples on supercomputers, we were able to prove that our three-scale parallel homogenisation analysis almost achieves the optimal acceleration ratio in parallel computing. Considering waviness as an initial irregularity in the carbon fibre arrangement, we then explored how it affects the macro-scale characteristics of FW-CFRP in fibre bundle tapes. We found that the waviness of the fibre significantly affects the macroscopic stress and stiffness when we analysed fibre abnormalities. In this investigation, compared to findings without irregularities, macroscopic stiffness was 40% lower and stress was 57% lower.

Keywords: Homogenization method, Carbon fiber-reinforced plastic (CFRP), High-pressure tank, Filament wind- ing, Winding misalignment, Finite element method, Parallel computation, Domain decomposition

1. Introduction

Fuel-cell vehicles are expected to gain increasing popularity owing to their minimal environmental footprints and expeditious refueling capabilities. The pivotal factor in their widespread adoption is enhancing their long-range cruising ability. However, considering the low energy density of hydrogen as a fuel source, it is imperative to integrate high-pressure hydrogen storage tanks. Such tanks require superior pressure endurance compared to traditional natural gas containers and must be lightweight to boost energy efficiency. A feasible solution to this challenge is the adoption of composite high-pressure storage vessels that combine durability with reduced weight. Composite high-pressure hydrogen storage vessels utilize various materials for structural integrity, including a plastic liner layer for hydrogen containment and carbon-fiber-reinforced plastic (CFRP) layer for pressure resistance. The primary component is the CFRP layer, which is formed using the filament winding (FW) method and plays a crucial role in maintaining overall structural strength.

The FW technique involves winding fiber bundle tapes around a curved surface with varying orientations, as shown in Fig. 1. The rigidity of vessels fluctuates significantly based on the winding pattern and number of fibers involved (Lisboa et al., 2020). When designing high-pressure vessels, assessing the material strength of CFRP layers shaped using the FW method is vital. Traditional methods for evaluating material strength typically involve extensive tensile and fatigue testing. However, strength evaluation tests that replicate actual machinery involve substantial production costs and extensive testing durations. Based on recent advancements, numerical simulation methods such as the finite element method (FEM) and homogenization method have led to the adoption of simulation-based approaches to evaluating the strength of practical structures.

Given the microscale heterogeneity within FW-CFRPs, developing a strength evaluation method that accounts for internal structures, including not only the winding structures of fiber bundle tapes but also the fibers and resins in tapes, is crucial for performing more detailed and advanced analysis. However, the analysis of the microstructure of an entire storage tank is computationally impractical. Homogenization methods are often employed for evaluating heterogeneous materials and material constants are determined by treating the region of interest as a homogenous domain (Wu and Ohno, 1999; Ohno et al., 2001; Terada and Kikuchi, 2001). An FW-CFRP is a composite material consisting of fibers that can be considered as a linear elastic and resin with material nonlinearity. Therefore, ordinary elastic analysis is insufficient for reproducing the associated mechanical behaviors and an analysis that considers the material nonlinearity of resin is required.

To evaluate the structural integrity of composite high-pressure vessels, assessing the impact of the initial irregularities occurring during formation on strength is also crucial. Specifically, fiber waviness is a key initial irregularity that has not been considered in the literature.

Some numerical simulations of FW composites based on FEM analyses have been conducted previously. Harada et al. (2018) performed burst tests on a Type-III FW tank, which had the same construction as an actual hydrogen tank, and in combination with FEM analyses, their findings revealed that the fiber volume fraction in the internal structure can affect strength. Lisboa et al. (2020) and Stabla et al. (2021, 2022) evaluated the effect of the winding pattern and winding angle on the strength and stiffness of FW composite tubes by performing compression tests and FEM analysis. Ye et al. (2020) investigated the periodic structures present in the winding patterns of FW-CFRPs. Zhang et al. (2008) proposed a periodic structure to match winding patterns and applied it to a mesoscopic FEM model with crimped fiber bundles, and Pourahmadi and Taheri-Behrooz (2020) proposed a mesoscopic FEM model and conducted macroscopic FEM simulations.

Homogenization analysis methods have been developed for textile composites to handle the material nonlinearity of resins, and elasto-viscoplastic and thermo-elasto-viscoplastic analyses of textile composites have been conducted (Matsuda et al., 2007; Matsuda et al., 2011; Kubo et al., 2019; Kubo et al., 2018). However, these studies did not consider initial irregularities such as fiber waviness. In contrast, we address the unit cell structure characteristics of the FW method through three-scale homogenization analysis by modeling a high-pressure hydrogen container at the macro-, meso-, and micro-scales (Fig. 2), where the fiber waviness in fiber bundle tapes is considered explicitly. However, numerical simulations that account for fiber waviness require high-resolution meshes to represent the fiber waviness wavelength, increasing computational demands, even with homogenization methods. Therefore, implementing parallel computation algorithms in multiscale analysis is imperative for reducing the computation time and enhancing the practicality of the proposed method.

Specifically, a three-scale inelastic homogenization analysis simulator for a high-pressure hydrogen storage vessel composed of a composite material using the FW method was developed. The developed simulator homogenizes the winding pattern of the FW method by considering fiber waviness in the mesoscale structure as an initial fiber waviness and evaluating its impact on macroscale material constants. To handle the increased computational scale of simulations considering fiber waviness, a parallel computation algorithm based on domain decomposition is proposed to improve the feasibility of the proposed numerical analysis method.

2. Overview of homogenization analysis

2.1. Governing equation of macroscale domain

Although this study aimed to implement a three-scale homogenization simulator, we first focus on a two-scale homogenization method consisting of the macro- and microscales, and provide a brief overview of homogenization analysis. Within the scope of this study, we consider an infinitesimal deformation and define a Cartesian coordinate system $\boldsymbol{x}$ in a macroscopic problem. When no volumetric forces are applied, the equilibrium of the macroscopic stress in the form of

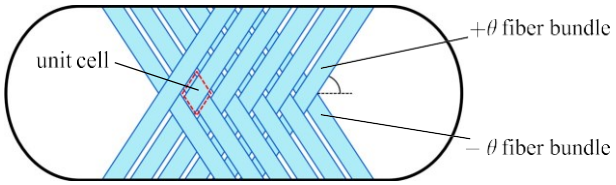

Fig. 1 Schematic representation of FW pattern. Fiber bundles are wrapped around the liner, and a stacking pattern with a periodic structure is obtained.

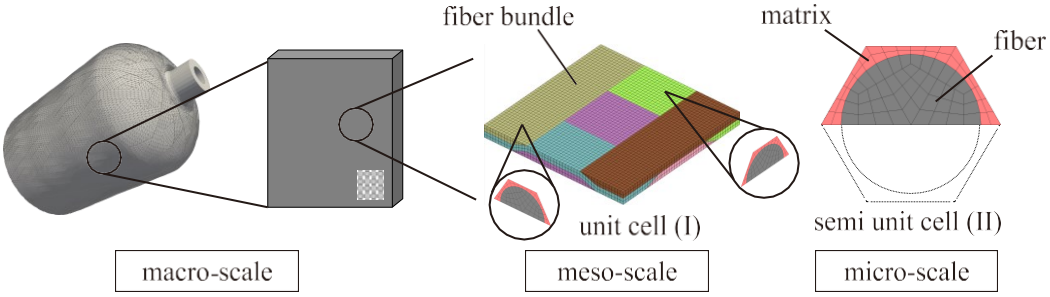

Fig. 2 Schematic representation of three scale homogenization method. Mesoscale unit cell (I) resolves fiber bundles, and microscale semi unit cell (II) resolves carbon fibers and resins.

velocity is represented as

$$\dot{\Sigma}_{ij,x_j} = 0, \tag{1}$$

where $\dot{\Sigma}$ is the macroscopic stress tensor, $(\dot{})$ is the time derivative, and the subscript $()_{,x_j}$ is the partial derivative with respect to the Cartesian coordinate $\boldsymbol{x}_j$.

Given the assumption that the domain Ω_x is composed of a periodic structure of elasto-viscoplastic materials, the homogenized elasto-viscoplastic properties are formulated as

$$\dot{\Sigma}_{ij} = C^{\mathrm{H}}_{ijkl}\,(\dot{E}_{kl} - \beta^{\mathrm{H}}_{kl}), \tag{2}$$

where $\dot{E}_{ij}$ is the macroscopic strain tensor, C^{H}_{ijkl} is the macroscopic elastic stiffness tensor, and β^{H}_{kl} is the macroscopic viscoplastic function tensor.

To apply the weighted residual method to the equilibrium of macroscopic stress, Eq. (1) is multiplied by the virtual displacement velocity $\delta\dot{U}_i$ and the weak form is derived as

$$\int_{\Omega_x} \dot{\Sigma}_{ij}\,\delta\dot{U}_{i,x_j}\mathrm{d}\Omega_x = \int_{\Gamma_x} \delta\dot{U}_i\,t_i\,\mathrm{d}\Gamma_x, \tag{3}$$

where $\boldsymbol{t}$ is the traction vector.

The equation (3) can be solved using the FEM. However, at this stage, the macroscopic elastic stiffness tensor C^{H}_{ijkl} and the macroscopic viscoplastic function β^{H}_{kl} are unknown. These values are determined by solving a microscopic problem using unit cells and averaging operations.

2.2. Governing equation of the microscale domain

In the microscale problem, where y denotes the Cartesian coordinate system, we focus on deriving the macroscopic elastic stiffness tensor C^{H}_{ijkl} and macroscopic viscoplasticity function β^{H}_{kl} to address the macroscale problem. Considering a unit cell Y, when there are no volumetric forces, the equilibrium of microscopic stress in its velocity form is described as

$$\dot{\sigma}_{ij,\mathsf{y}_j} = 0, \tag{4}$$

where $\dot{\sigma}_{ij}$ is the microscopic stress rate.

The microscopic displacement velocity $\dot{u}_i(\mathsf{y})$ in the unit cell Y is expressed as

$$\dot{u}_i(\mathsf{y}) = \dot{E}_{ij}\,\mathsf{y}_j + \dot{u}^{\#}_i(\mathsf{y}). \tag{5}$$

Here, the first term on the right side represents the macroscopic uniform deformation and the second term represents the disturbance displacement. $\dot{u}^{\#}_i(\mathsf{y})$ is $Y-$periodic term and is distributed within unit cell Y.

The microscopic strain rate $\dot{\varepsilon}_{ij}$ is expressed as

$$\dot{\varepsilon}_{ij}(\mathbf{y}) = \dot{E}_{ij} + \dot{\varepsilon}^{\#}_{ij}(\mathbf{y}), \tag{6}$$

where the disturbance strain rate $\dot{\varepsilon}^{\#}_{ij}$ is expressed as

$$\dot{\varepsilon}^{\#}_{ij} = \frac{1}{2}\{\dot{u}^{\#}_{i,y_j} + \dot{u}^{\#}_{j,y_i}\}. \tag{7}$$

Assuming that the periodic domain Y consists of elasto-viscoplastic materials, the elasto-plastic properties are expressed as

$$\dot{\sigma}_{ij} = C_{ijkl}(\dot{\varepsilon}_{kl} - \beta_{kl}), \tag{8}$$

where C_{ijkl} is the microscopic elastic stiffness tensor, and β_{kl} is the microscopic viscoplastic function. The viscoplasticity function β_{kl} follows Norton's rule as

$$\beta_{ij} = \frac{3}{2}\dot{\varepsilon}^{p}_{0}\left\{\frac{\bar{\sigma}}{g(\bar{\varepsilon}^{p})}\right\}^{n}\frac{s_{ij}}{\bar{\sigma}}, \tag{9}$$

where n is the material constant of the resin, g is the hardening function, $\bar{\varepsilon}^{p}$ is the equivalent viscoplastic strain, $\dot{\varepsilon}^{p}_{0}$ is the reference strain rate, s_{ij} is the deviatoric stress and $\bar{\sigma}$ is the equivalent stress.

By multiplying the equilibrium microscopic stress in Eq. (4) by the variation $\boldsymbol{v}$ and integrating over the domain Y, the following weak form is obtained:

$$\int_Y \dot{\sigma}_{ij}\,\delta v_{i,y_j}\,d\Omega_y = \int_{\Gamma_y} v_i\,t_i\,d\Gamma_y, \tag{10}$$

where the right side is zero if Y-periodicity is satisfied because its normals are oriented in opposite directions on opposite boundaries.

By substituting Eq. (5), to (8) into Eq. (10) and reorganizing, we obtain the following equation:

$$\int_Y C_{ijpq}\,\dot{u}^{\#}_{p,y_q}\,v_{i,y_j}\,dY = -\dot{E}_{kl}\int_Y C_{ijkl}\,v_{i,y_j}\,dY + \int_Y C_{ijkl}\,\beta_{kl}\,v_{i,y_j}\,dY. \tag{11}$$

Assuming that Eq. (11) is linearized, the disturbance displacement velocity field $\dot{u}^{\#}_{i}$, which is the solution to the boundary value problem, can be expressed in the following functional form using the Y-periodic characteristic functions χ^{kl}_{i} and ϕ_i:

$$\dot{u}^{\#}_{i}(\mathbf{y}) = \chi^{kl}_{i}(\mathbf{y})\dot{E}_{kl} + \phi_i(\mathbf{y}). \tag{12}$$

Consequently, the characteristic functions χ^{kl}_{i} and ϕ_i are obtained by solving the following boundary value problems:

$$\int_Y C_{ijpq}\,\chi^{kl}_{p,y_q}\,v_{i,y_j}\,dY = -\int_Y C_{ijkl}\,v_{i,y_j}\,dY, \tag{13}$$

$$\int_Y C_{ijpq}\,\phi_{p,y_q}\,v_{i,y_j}\,dY = \int_Y C_{ijkl}\,\beta_{kl}\,v_{i,y_j}\,dY. \tag{14}$$

Substituting Eqs. (6) and (12) into Eq. (8) yields

$$\dot{\sigma}_{ij} = C_{ijpq}\left(\delta_{pk}\delta_{ql} + \chi^{kl}_{p,y_q}\right)\dot{E}_{kl} - C_{ijkl}\left(\beta_{kl} - \phi_{k,y_l}\right). \tag{15}$$

2.3. Homogenization of microscale material properties

By leveraging the volume-averaging operation of the homogenization method, the macroscopic material constant can be derived using the following equation:

$$\dot{\Sigma}_{ij} = \left\langle C_{ijpq}\left(\delta_{pk}\delta_{ql} + \chi^{kl}_{p,y_q}\right)\right\rangle\dot{E}_{kl} - \left\langle C_{ijkl}\left(\beta_{kl} + \phi_{k,y_l}\right)\right\rangle, \tag{16}$$

where δ_{ij} is the Kronecker delta. The average volume with respect to the unit cell is defined as

$$\langle \# \rangle = \frac{1}{|Y|}\int_Y \# \, dY, \tag{17}$$

where $|Y|$ is the volume of the unit cell.

Similarly, the macroscopic strain rate and stress rate are expressed as follows:

$$\dot{E}_{ij} = \langle \dot{\varepsilon}_{ij} \rangle, \tag{18}$$

$$\dot{\Sigma}_{ij} = \langle \dot{\sigma}_{ij} \rangle. \tag{19}$$

3. Proposed method: parallel three-scale homogenization

3.1. Three-scale homogenization algorithm

The structure of the target FW-CFRP was modeled using the three-scale model shown in Fig. 2 and the unit cells were constructed from periodic structures at the mesoscopic and microscopic scales. A unit cell (I) consisting of two types of fiber bundles, i.e straight and crimped fiber bundles, was defined on the mesoscopic scale and a semi unit cell (II) consisting of a fiber and resin was defined on the microscopic scale. For each unit cell, we again define the Cartesian coordinate systems $\boldsymbol{x}$ and $\boldsymbol{y}$. Physical quantities at the macro-, meso-, and microscales are assigned superscripts of 0, 1, and 2, respectively.

The mesoscopic-microscopic homogenization scheme is applied to the stress and strain in the micro unit cell (II), which are represented as ${}^2\sigma_{ij}$ and ${}^2\varepsilon_{ij}$, respectively. Then, the evolution equation of ${}^2\sigma_{ij}$ is derived in the same form as Eq. (15) as

$$ {}^2\dot{\sigma}_{ij} = {}^2C_{ijpq}\left(\delta_{pk}\delta_{ql} + {}^2\chi^{kl}_{p,y_q}\right){}^1\dot{\varepsilon}_{kl} - {}^2C_{ijkl}\left({}^2\beta_{kl} - {}^2\phi_{k,y_l}\right), \tag{20} $$

where ${}^2\chi^{kl}_i$ and ${}^2\phi_i$ are determined by solving the following boundary value problems for the unit cell (II):

$$ \int_{Y_{\mathrm{II}}} {}^2C_{ijpq}\,{}^2\chi^{kl}_{p,y_q}\,v_{i,y_j}\,dY_{\mathrm{II}} = -\int_{Y_{\mathrm{II}}} {}^2C_{ijkl}\,v_{i,y_j}\,dY_{\mathrm{II}}, \tag{21} $$

$$ \int_{Y_{\mathrm{II}}} {}^2C_{ijpq}\,{}^2\phi_{p,y_q}\,v_{i,y_j}\,dY_{\mathrm{II}} = \int_{Y_{\mathrm{II}}} {}^2C_{ijkl}\,{}^2\beta_{kl}\,v_{i,y_j}\,dY_{\mathrm{II}}. \tag{22} $$

By taking the volume average $\langle\rangle_{\mathrm{II}}$ with respect to the microscopic unit cell (II) in Eq. (20), the following constitutive equation for fiber bundle tapes can be derived at the mesoscale:

$$ {}^1\dot{\sigma}_{ij} = \left\langle {}^2C_{ijpq}\left(\delta_{pk}\delta_{ql} + {}^2\chi^{kl}_{p,y_q}\right)\right\rangle_{\mathrm{II}}{}^1\dot{\varepsilon}_{kl} - \left\langle {}^2C_{ijkl}\left({}^2\beta_{kl} - {}^2\phi_{k,y_l}\right)\right\rangle_{\mathrm{II}}. \tag{23} $$

Similarly, by applying homogenization theory to the macroscopic-mesoscopic homogenization scheme, we obtain the equation of mesoscopic stress and the macroscopic constitutive equation of the FW-CFRP as shown in Eqs. (24) and (25).

$$ {}^1\dot{\sigma}_{ij} = {}^1C_{ijpq}\left(\delta_{pk}\delta_{ql} + {}^1\chi^{kl}_{p,x_q}\right){}^0\dot{\varepsilon}_{kl} - {}^1C_{ijkl}\left({}^1\beta_{kl} - {}^1\phi_{k,x_l}\right) \tag{24} $$

$$ {}^0\dot{\sigma}_{ij} = \left\langle {}^1C_{ijpq}\left(\delta_{pk}\delta_{ql} + {}^1\chi^{kl}_{p,x_q}\right)\right\rangle_{\mathrm{I}}{}^0\dot{\varepsilon}_{kl} - \left\langle {}^1C_{ijkl}\left({}^1\beta_{kl} - {}^1\phi_{k,x_l}\right)\right\rangle_{\mathrm{I}} \tag{25} $$

Here, $\langle\rangle_{\mathrm{I}}$ is the volume average with respect to the mesoscopic unit cell (I), and ${}^1\chi^{kl}_i$ and ${}^1\phi_i$ are determined by solving the following boundary value problems for the unit cell (I):

$$ \int_{Y_{\mathrm{I}}} {}^1C_{ijpq}\,{}^1\chi^{kl}_{p,y_q}\,v_{i,y_j}\,dY_{\mathrm{I}} = -\int_{Y_{\mathrm{I}}} {}^1C_{ijkl}\,v_{i,y_j}\,dY_{\mathrm{I}}, \tag{26} $$

$$ \int_{Y_{\mathrm{I}}} {}^1C_{ijpq}\,{}^1\phi_{p,y_q}\,v_{i,y_j}\,dY_{\mathrm{I}} = \int_{Y_{\mathrm{I}}} {}^1C_{ijkl}\,{}^1\beta_{kl}\,v_{i,y_j}\,dY_{\mathrm{I}}. \tag{27} $$

It should be noted that ${}^1C_{ijkl}$ and ${}^1C_{ijkl}{}^1\beta_{kl}$ in the above equations have the following relationships with the averaged quantities in Eq. (23):

$$ {}^1C_{ijkl} = \left\langle {}^2C_{ijpq}\left(\delta_{pk}\delta_{ql} + {}^2\chi^{kl}_{p,y_q}\right)\right\rangle_{\mathrm{II}}, \tag{28} $$

$$ {}^1C_{ijkl}{}^1\beta_{kl} = \left\langle {}^2C_{ijkl}\left({}^2\beta_{kl} - {}^2\phi_{k,y_l}\right)\right\rangle_{\mathrm{II}}, \tag{29} $$

which enables to couple mesoscopic-microscopic and macroscopic-mesoscopic homogenization schemes. It should also be noted that the coordinate rotation is appropriately given to $\left\langle {}^2C_{ijpq}\left(\delta_{pk}\delta_{ql} + {}^2\chi^{kl}_{p,y_q}\right)\right\rangle_{\mathrm{II}}$ and $\left\langle {}^2C_{ijkl}\left({}^2\beta_{kl} - {}^2\phi_{k,y_l}\right)\right\rangle_{\mathrm{II}}$ in Eqs. (28) and (29) according to the directions of the fibers in the fiber bundle tapes.

3.2. Parallel computation based on domain decomposition

In scenarios where the analysis target requires a fine mesh, the resultant increase in the computation scale leads to an escalation in both computation time and memory usage. With sequential calculations on a shared-memory computer, the computation time becomes excessive or the computational process hits the memory capacity limit, rendering further calculations unfeasible.

The advantage of the proposed approach is that it reduces computation time by utilizing multiple computation cores. Additionally, it helps alleviate memory capacity constraints, particularly when implemented on distributed-memory parallel computers such as supercomputers. However, a notable consideration with distributed-memory parallel computers

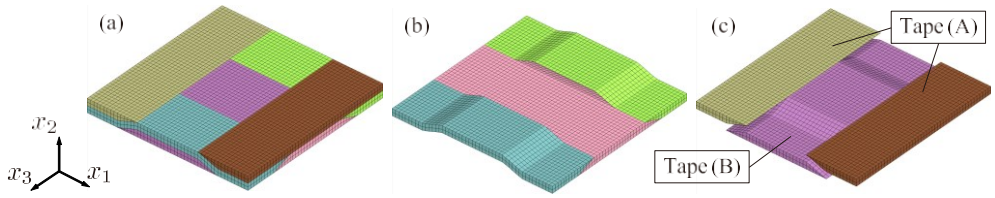

Fig. 3 Analysis mesh of mesoscopic model. The mesoscale unit cell (a) consists of straight tape and tapes with crimp. Tapes which fiber orientation coincides with the x_1 direction are shown in (b), and tapes in which fiber orientation coincides with the x_3 direction are shown in (c).

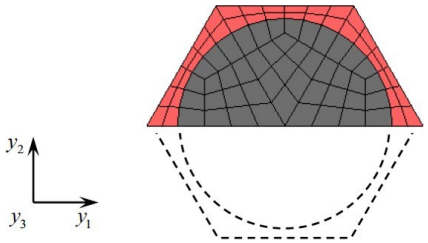

Fig. 4 Analysis mesh of microscopic model. The microscale semi unit cell resolves resin and carbon fibers separately.

is the absence of shared memory coupled with limited memory capacity per computer node. Consequently, large datasets must be partitioned preemptively.

One data partitioning method is based on domain decomposition, where a finite element mesh is spatially partitioned. In the FEM, interaction (exchange of information) occurs among the nodes that compose the mesh. Therefore, it is reasonable to consider spatial decomposition during data partitioning. In this study, domain decomposition was performed using mesoscopic meshes. In mesoscopic meshes, multiple cores communicate with each other via domain decomposition. Additionally, the mesh representing the microscopic structure is tied to the integration points of the mesoscopic mesh. As a result, there is no need for data communication between domains, which can be computed independently; this is expected to result in high computational efficiency.

For mesh partitioning, the mesh was considered as a graph and the minimum-cut problem was solved. The graph minimum-cut problem minimizes the number of edges (connections between nodes) across partitioned subdomains under the constraint that the number of nodes belonging to each partitioned subdomain is equal. By keeping the number of nodes equal in each subdomain, the load balance is maintained during parallel computation. Minimizing the number of edges that straddle the divided subdomains minimizes the amount of data communication required between subdomains. Such subdomain partitioning is expected to yield high parallel computation efficiency. In this implementation, fortran90 and Intel compiler (2020.4.304) were used as programming language, and the METIS software was used for graph partitioning (Karypis and Kumar, 1997). For parallel implementation, the domain-decomposition-based parallel linear solver library Monolis was adopted (Monolis, 2023).

4. Performance evaluation of parallel three-scale homogenization analysis

The parallel computation performance of the developed three-scale homogenization simulator was evaluated in terms of strong scaling performance (Breshears, 2009). Strong scaling evaluates the acceleration ratio of the computation time when the number of CPU cores used for parallel computation is increased while maintaining the number of mesh nodes. The acceleration ratio S_n is defined as follows:

$$S_n = t_1/t_n, \tag{30}$$

where S_n is the acceleration ratio when the number of parallelizations (i.e., number of subdomains) is n, t_n is the calculation time when the number of parallelizations is n, and t_1 is the calculation time (i.e., sequential computation time) when the number of parallelizations is one. If strong scaling performance is achieved, then the computation time can be efficiently reduced, which is expected to improve the utility of the simulator.

Coarse and fine computational models were created as mesoscopic structures. The meshes used were hexahedral first-order elements. The mesoscopic mesh used in the coarse model contained 13,965 nodes and 11,136 elements (Fig.

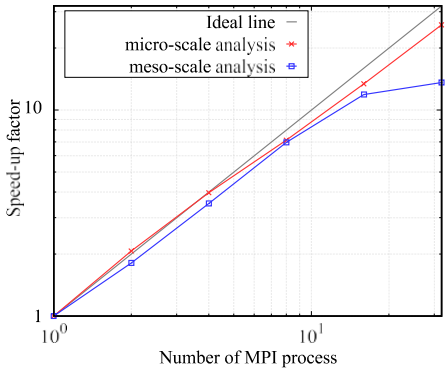

Fig. 5 Acceleration ratio of three-scale analysis (coarse model). The good acceleration ratio is observed for microscopic analysis. In contrast, the improvement in acceleration performance slowed for mesoscopic analysis at 32 parallel processes. Microscopic analysis does not require data communication between parallel processes and each process can be computed independently. However, mesoscopic analysis requires data communication between parallel processes.

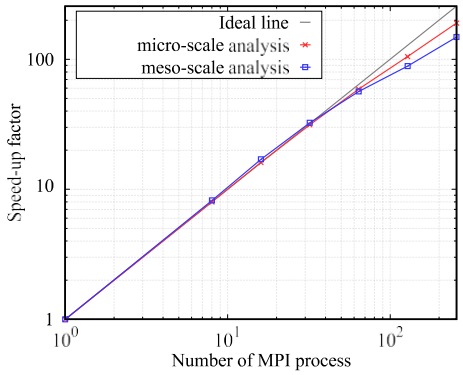

Fig. 6 Acceleration ratio of three-scale analysis (fine model). The good acceleration ratios are observed for both microscopic and mesoscopic analysis. As the number of mesh nodes increases, the amount of computation that each process can handle increases, which decreases the ratio of computation time required for data communication.

3). The fine model contained 100,201 nodes and 89,088 elements. The fine model was obtained by refining the hexahedral elements of the coarse model. The same mesh was used for the microscopic structures in both models, as shown in Fig. 4. This mesh assumes a generalized plane strain state and uses quadrilateral first-order elements. The microscopic meshes had 81 nodes, 97 elements, and 73% fiber volume content.

The material constants for carbon fiber, which acts as a transversely isotropic elastic material, are listed in Table 1 (TORAY CFE, 2023). The constants for the epoxy resin, which acts as an isotropic elasto-viscoplastic material, are listed in Table 2 (Takahashi et al., 2022).

Boundary conditions simulating uniaxial tension with deformation control were applied to the models. Uniaxial tension with a macroscopic constant strain rate of ${}^0\dot{\varepsilon}_{33} = 1.1 \times 10^{-4}\ s^{-1}$ was defined and calculated for one step with $\Delta t = 1.0$ s. The equations to be solved for the mesoscopic structure were obtained using the conjugate gradient method and diagonal scaling preconditioning. The equations for the microscopic structure were solved efficiently by assuming the same microstructure mesh, using the sparse matrix direct method library MUMPS (Amestoy et al., 2000), and storing the results of LU decomposition. An Oakbridge CX supercomputer at the University of Tokyo was used for computation (Oakbridge CX, 2023). The computation times were measured in the range of 1 to 32 parallel processes for the coarse model and in the range of 1 to 256 parallel processes for the fine model. For the coarse model, calculations were performed

Table 1 Material constants of carbon fibers

E_{LL} [GPa]	264
E_{TT} [GPa]	19.0
ν_{LT}	0.28
ν_{TT}	0.49
G_{LT} [GPa]	56.0

Table 2 Material constants of epoxy resin

E_m [GPa]	2.7
ν_m	0.35
$\dot{\varepsilon}_0^p$ $[s^{-1}]$	1.0×10^{-5}
n	25
$g(\bar{\varepsilon}^p)$	$122.8(\bar{\varepsilon}^p)^{0.228} + 0.5$

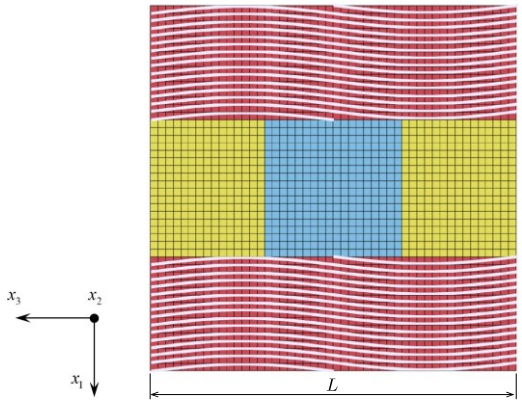

Fig. 7 Schematic representation of fiber waviness. The reduction of macroscopic stiffness due to waviness is simulated by controlling the direction of fiber orientation in the microscopic model, which is assigned to the mesoscopic model.

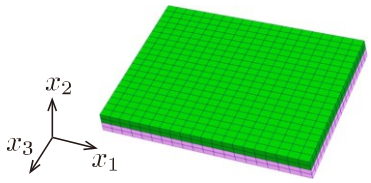

Fig. 8 Analysis mesh of straight tape model used for comparison with experimental results. This model has no fiber bundle crimps.

for one computation node. For the fine model, six CPU cores were used per computation node and the number of computation nodes used was determined accordingly.

Figure 5 presents the strong scaling performance of the coarse model. The breakdown of the total computation time for the sequential computation of the coarse model was 34.3 s for microscopic analysis and 37.0 s for mesoscopic analysis. The horizontal axis represents the number of cores used for parallel computation, which is consistent with the number of domains. The red line represents the acceleration ratio for microscopic analysis, blue line represents the acceleration ratio for mesoscopic analysis, and black line represents the ideal acceleration performance. Figure 5 reveals that the ideal acceleration ratios were observed for 1 to 16 parallel processes. In contrast, 32 parallel processes yielded a good acceleration ratio for microscopic analysis, but the improvement in acceleration performance slowed for mesoscopic analysis. While microscopic analysis does not require data communication between parallel processes and each process can be computed independently, mesoscopic analysis requires data communication between parallel processes. As the number of parallel processes increases, the amount of computation that each process can handle decreases, which increases the ratio of computation time required for data communication.

Figure 6 presents the strong scaling performance of the fine model. The total computation time for sequential computation was 288.0 s for microscopic analysis and 706.0 s for mesoscopic analysis. The presented results highlight the effectiveness of the parallel computation of the developed three-scale homogenization simulator.

5. Multi-scale modeling of FW-CFRP considering fiber waviness

Our parallel three-scale homogenization simulator was used to evaluate the effect of manufacturing errors at the mesoscopic scale on the macroscopic stress–strain relationship. The model presented in Fig. 3 was used for the meso-scopic structure and the two-dimensional mesh presented in Fig. 4 was used for the microscopic structure. Uniaxial tension was applied at a macroscopic constant strain rate of ${}^{0}\dot{\varepsilon}_{33} = 1.1 \times 10^{-4}\mathrm{s}^{-1}$ until $\varepsilon_{33} = 1.5\%$. The time increment was $\Delta t = 1.0$ s. The material constants described in Section 4 were adopted.

To evaluate the effects of fiber irregularities on the macroscopic stiffness and stress level, we considered the fiber waviness in a fiber bundle tape (Ueda et al., 2024). Figure 7 presents a schematic representation of fiber waviness in the x_3 direction. Assuming that the direction of the fiber orientation can be approximated by a trigonometric function, the

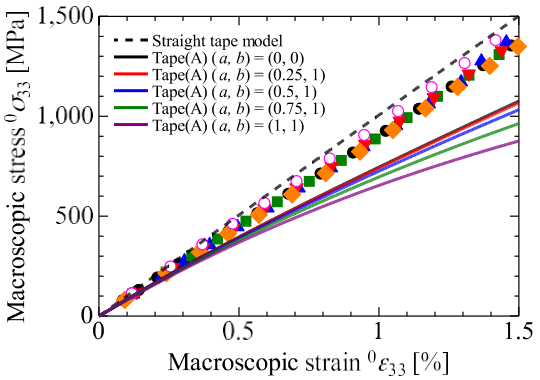

Fig. 9 Macroscopic stress-strain relationship of FW-CFRP with fiber waviness in Tape (A) (effect of amplitude). As the amplitude a increases, both stiffness and stress tend to decrease.

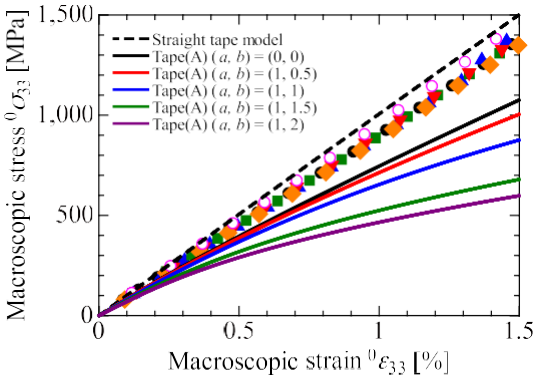

Fig. 10 Macroscopic stress-strain relationship of FW-CFRP with fiber waviness in Tape (A) (effect of the number of waves). As the wavenumber b increases, both the stiffness and stress tend to decrease.

waviness w is defined as

$$w = al \sin\left(\frac{2b\pi x_i}{L}\right), \tag{31}$$

where l is the representative width of one element, L is the width of the mesoscopic unit cell, x_i is coordinate of the x_i direction, a is the magnification factor with respect to the amplitude, and b is the number of waves. For example, when a = 1, an initial fiber waviness occurs such that there is a one-element shift in the orthogonal in-plane direction from the original fiber orientation direction. The mesoscopic material properties (shown in Eq. (23)) in elements with waviness are transformed into appropriate coordinates according to the wave angle.

As a basic investigation, we evaluated the effect of fiber waviness on mechanical response under simple tensile conditions for straight tapes (A) in the x_3 direction and crimped tapes (B) in the x_3 direction among the four fiber bundle tapes that constitute a mesoscopic unit cell. Tensile tests were conducted on the FW-CFRP specimens to validate our numerical calculations (Takahashi et al., 2022). Specimens with a $[0/90]_{2s}$ laminate configuration were formed by wrapping fiber bundle tape around a jig using the FW method. When cut, the specimen dimensions were in accordance with the JISK7165 standard. The tensile test results are presented as dots in Figs. 9 to 14. It should be noted that the fiber bundle tapes in the specimens had no crimp, dissimilar to the mesoscopic model presented in Fig. 3. All of the tapes were straight because the 0° and 90° layers were wound alternately. Therefore, we created a mesoscopic model with straight tapes (called the 'straight tape model' shown in Fig. 8) and subjected it to three-scale analysis, resulting in the stress–strain relationship indicated by the dashed lines in Figs. 9 to 14. One can see that the dashed lines are in good agreement with the experimental data, validating the proposed analysis method and the material constants described in Section 4.

5.1. Effect of fiber waviness in straight tapes (A) on macroscale property

First, we evaluate the effect of fiber irregularities in the x_3-directed straight tape (A) on the corresponding macroscopic stress–strain relationship. Figure 9 presents the stress–strain relationships obtained on the macroscale when the wavenumber b was fixed at one and the amplitude factor a was varied with values of 0.25, 0.5, 0.75, and 1, as well as

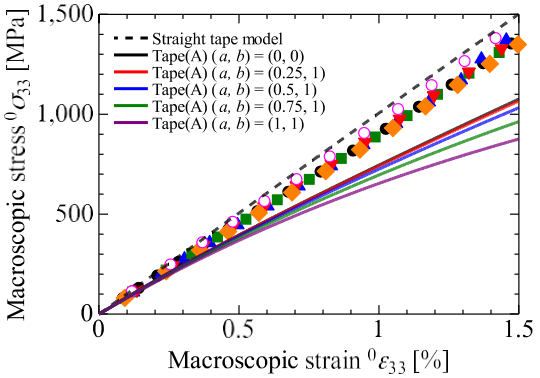

Fig. 11 Macroscopic stress-strain relationship of FW-CFRP with fiber waviness in Tape (B) (effect of amplitude). The change in the stress–strain diagrams is very small compared to the case of tape (A) as shown in Fig. 9.

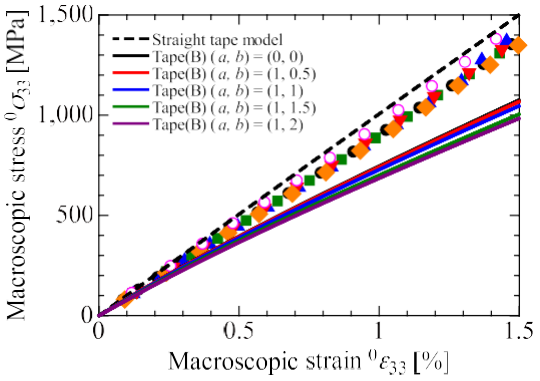

Fig. 12 Macroscopic stress-strain relationship of FW-CFRP with fiber waviness in Tape (B) (effect of the number of waves). The change in the stress–strain diagrams is quite small compared to the case of Tape (A) as shown in Fig. 10.

the results for the case without fiber waviness (i.e., $(a, b) = (0, 0)$). One can see that the stiffness and stress levels for $(a, b) = (0, 0)$ are slightly lower than those of the experimental data and straight tape model due to the effects of crimps in the fiber bundle tapes. When comparing the stress–strain relationships for the cases with fiber waviness to one another, as the amplitude a increases, the difference in the angle between the direction of carbon fiber orientation and the tensile direction increases. As a result, both stiffness and stress tend to decrease. In the case of $(a, b) = (1,1)$, the stiffness and stress decreased by 4.8% and 12.3%, respectively, compared to the results without irregularities at 1% macroscopic strain.

Figure 10 presents the macroscopic stress-strain relationships when the amplitude a was fixed at one and the wavenumber b varied with values of 0.5, 1, 1.5, and 2. One can see that both the stiffness and stress tend to decrease as the wavenumber b increases. This is because the angle between the direction of carbon fiber orientation and the tensile direction is larger when the wave number b increases within the range of the parameters examined in this study. In the case of $(a, b) = (1,2)$, the stiffness and stress were reduced by 16.5% and 37.6%, respectively, at 1% macroscopic strain compared to the results with no irregularities.

5.2. Effect of fiber waviness in crimped tapes (B) on macroscale property

In this section, we evaluate the effects of fiber irregularities in the x_3-directed crimped tape (B) on the corresponding macroscopic stress–strain relationship. Figure 11 presents the macroscopic stress–strain relationships obtained when the wavenumber b was fixed at one and the amplitude factor a was varied with values of 0.25, 0.5, 0.75, and 1. Figure 12 presents the stress–strain relationships obtained at the macroscale when the amplitude a was fixed at one and the wavenumber b was varied with values of 0.5, 1, 1.5, and 2. In these figures, one can see that the change in the stress–strain diagrams is very small compared to the case where tape (A) was given a fiber waviness in the previous subsection. This is because the original model has crimps that avoid the straight tape (A). Therefore, tape (B) is not subjected to stress and even if the fiber waviness reduces the stiffness of the tape (B) section, the effect on the macroscopic level is small.

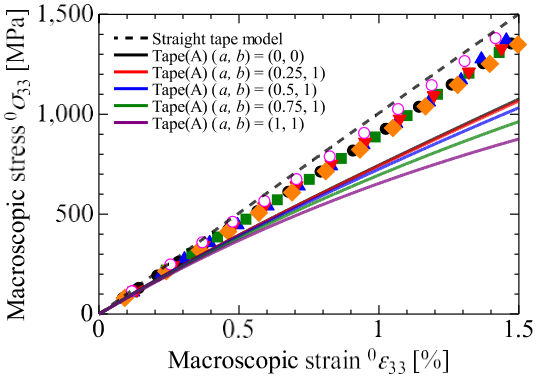

Fig. 13 Macroscopic stress-strain relationship of FW-CFRP with fiber waviness in Tape (A) and Tape (B) (effect of amplitude). The stiffness and stress are lower compared to the case when fiver waviness was considered only for Tape (A) (Fig. 9) or Tape (B) (Fig. 11).

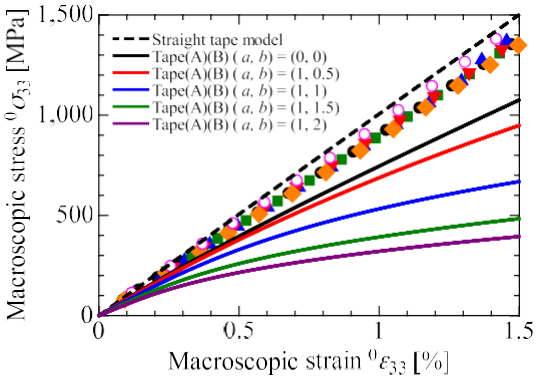

Fig. 14 Macroscopic stress-strain relationship of FW-CFRP with fiber waviness in Tape (A) and Tape (B) (effect of the number of waves). The stiffness and stress decreased the most under all conditions.

5.3. Effect of fiber waviness in straight tapes (A) and crimped tapes (B) on macroscale property

In this section, we evaluate the effects of fiber irregularities in both the straight tape (A) and crimped tape (B) on the corresponding macroscopic stress–strain relationships. Figure 13 presents the macroscopic stress–strain relationships obtained when the wavenumber b was fixed at one and the amplitude factor a was varied with values of 0.25, 0.5, 0.75, and 1. One can see that the stiffness and stress are much lower compared to the case when irregularities were considered only for tape (A). These reductions are not a direct result of the addition of irregularities to both tapes (A) and (B), but rather a result of the fact that the load is applied from tape (A) to tape (B) because when both tapes have irregularities, it results in a superimposed phenomenon of stiffness and stress reduction. In the case of (a, b) = (1,1), the stiffness and stress decreased by 11.3% and 28.6%, respectively, at 1% macroscopic strain compared to the results without irregularities.

Figure 14 presents the stress–strain relationships obtained at the macroscale when the amplitude a was fixed at one and the wavenumber b is varied with values of 0.5, 1, 1.5, and 2. One can see that the stiffness and stress decreased the most under these conditions. In the case of (a, b) = (1,2), the stiffness and stress decreased by 40.0 and 57.0%, respectively, at 1% macrostrain compared to the results without irregularities.

5.4. Discussion

Our investigation focused on the impact of irregularities in the straight tape (A) and crimped tape (B) on the stiffness and stress within a mesoscopic structure, specifically in the context of the homogenization of the winding pattern characteristics of the FW method.

The numerical results revealed that when employing a regular straight tape (A), the influence of the fiber waviness of the crimped tape (B) on the macroscopic stiffness and stress was relatively minor. In contrast, the presence of fiber waviness in both the straight tape (A) and crimped tape (B) led to a reduction in both stiffness and stress. Mitigating fiber waviness in both the straight tape (A) and crimped tape (B) during the shaping process of vessels requires advanced forming control technology. However, if only the fiber waviness within the straight tape (A) can be effectively reduced, then it may be possible to avert the compounded reduction in stiffness and stress induced by fiber waviness in both tapes.

6. Conclusions

In this work, a simulator for high-pressure hydrogen storage containers made using the FW approach was constructed. The simulator takes macro-, meso-, and microscale structures into account. Using this simulator, in-depth analyses that take fibre anomalies into account are made possible. In addition, we looked at how fibre waviness affected attributes at the macro scale by starting with a mesoscale structure with a homogenised winding pattern, where waviness was an initial irregularity in the carbon fibre arrangement. The results showed as follows.

• Through the use of large-scale models and numerical examples, it was confirmed that parallel three-scale homogenisation analysis achieves parallel computing performance that is near to the optimum acceleration ratio.
• The impact of fibre waviness on macroscopic stress and stiffness was found to be significant, according to analysis of fibre irregularities. Compared to findings without irregularities at 1% macrostrain, the stiffness was lowered by 40% and stress by 57% within the scope of this investigation.

• We looked at how macroscopic stiffness and stress were affected by straight tape (A) and crimped tape (B) imperfections. According to the findings, it is possible to avoid the combined effects of reduced stress and increased stiffness due to crimped tape (B) and straight tape (A) by smoothing out the fibres in the former.

Acknowledgement

This work was based on the results obtained from a project (JPNP20003) commissioned by the New Energy and Industrial Technology Development Organization (NEDO).

References

Amestoy, P. R., Duff, I. S., L'Excellent, J. Y. and Koster, J., MUMPS: a general purpose distributed memory sparse solver. International Workshop on Applied Parallel Computing (2000), pp. 121-130, Springer Berlin Heidelberg.

Breshears, C., The art of concurrency: A thread monkey's guide to writing parallel applications. O'Reilly Media, Inc., (2009).

Harada, S., Arai, Y., Araki, W., Iijima, T., Kurosawa, A., Ohbuchi, T. and Sasaki, N., A simplified method for predicting burst pressure of type III filament-wound CFRP composite vessels considering the inhomogeneity of fiber packing, Composite Structures, Vol. 190 (2018), pp. 79-90.

Karypis, G. and Kumar, V., METIS: A software package for partitioning unstructured graphs, partitioning meshes, and computing fill-reducing orderings of sparse matrices (1997).

Kubo, G., Matsuda, T., Nagaoka, H. and Sato, Y., Development and Validation of Multiscale Thermo-elasto-viscoplastic Analysis Method for Plain-Woven Composites, Key Engineering Materials, Vol. 794 (2019), pp. 78-88.

Kubo, G., Matsuda, T. and Sato, Y., A novel basic cell modeling method for elastic-viscoplastic homogenization analysis of plain-woven laminates with nesting, International Journal of Mechanical Sciences, Vol. 146-147(2018), pp. 497-506.

Lisbôa, T. V., Almeida, J. H. S., Dailibor, I. H., Spickenheuer, A., Marczak, R. J. and Amico, S.C., The role of winding pattern on filament wound composite cylinders under radial compression, Polymer composites, Vol.41 (2020), pp. 2446-2454.

Matsui, K., Terada, K. and Yuge, K., Two-scale finite element analysis of heterogeneous solids with periodic microstructures. Computers & structures, Vol. 82, No. 7-8 (2004), pp. 593-606.

Matsuda, T., Nimiya, Y., Ohno, N. and Tokuda, M., Elastic-viscoplastic behavior of plain-woven GFRP laminates: homogenization using a reduced domain of analysis, Composite Structures, No. 79 (2007), pp. 493-500

Matsuda, T., Kanamaru, S., Yamamoto, N. and Fukuda, Y., A homogenization theory for elastic-viscoplastic materials with misaligned internal structures, International Journal of Plasticity, No. 27 (2011), pp. 2056-2067

monolis: monolithic linear solver based on domain decomposition (online), available from <https://www.kz.tsukuba.ac.jp/nmorita/monolis.html>, (accessed on 30 November, 2023).

Oakbridge-CX (online), available from <https://www.cc.u-tokyo.ac.jp/supercomputer/obcx/service/>, (accessed on 30 November, 2023).

Ohno, N., Matsuda, T. and Wu, X., A homogenization theory for elastic-viscoplasitc composites with point symmetry of internal distribution, International Journal of Solids and Structures, Vol. 38 (2001), pp. 2867-2878.

Pourahmadi, E. and Taheri-Behrooz F., The influence of fiber bundle width on the mechanical properties of filament-wound cylindrical structures, International Journal of Mechanical Science, Vol. 178 (2020), DOI: 10.1016/j.ijmecsci.2020.105617.

Stabla, P., Smolnicki, M. and Blazejewski, W., The Numerical Approach to Mosaic Patterns in Filament-Wound Composite Pipes, Applied Composite Materials, Vol. 28 (2021), pp. 181-199.

Stabla, P., Lubecki, M. and Smolnicki, M., The effect of mosaic pattern and winding angle on radially compressed filamentwound CFRP composite tubes, Composite Structures, Vol. 292 (2022), DOI: 10.1016/j.compstruct.2022.115644.

Takahashi, T., Matsuda, T., Morita, N., Ueda, M., Yokozeki, T. and Iwase, W., Multiscale Inelastic Analysis of FW-CFRP for High-Pressure Hydrogen Tanks, 15th World Congress on Computational Mechanics and 8th Asian Pacific Congress on Computational Mechanics (2022), Paper No. MS0807-1617.

Terada, K. and Kikuchi, N., A class of general algorithms for multi-scale analyses of heterogeneous media. Computer methods in applied mechanics and engineering, Vol. 190, No. 40-41 (2001), pp. 5427-5464.

TORAY CFE (online), available from <https://toray-cfe.com/wp-content/uploads/2020/12/toray-torayca-fibers-typical-properties.pdf>, (accessed on 30 November, 2023).

Ueda, M., Hidaka, T., Ichihara, N., Yang, H., Iwase, W., Matsuda, T., Morita, N., Aoki, R. and Yokozeki. T., Voids in type-IV composite pressure vessels manufactured by a dry filament-winding process, International Journal of Pressure Vessels and Piping, No. 208 (2024), p.105154.

Wu, X. and Ohno N., A Homogenization Theory for Time-Dependent Nonlinear Composites with Periodic Internal Structure, International Journal of Solids and Structures, Vol. 36 (1999), pp. 4911-5012.

Ye, J., Yan, Y., Li, Y. and Luo, H., Parametric mesoscopic and multi-scale models for predicting the axial tensile response of filament-wound structures, Composite Structures, Vol. 242 (2020), DOI: 10.1016/j.compstruct.2020.112141.

Zhang, Y., Xia, Z. and Ellyin, F., Two-scale analysis of a filament-wound cylindrical structure and application of periodic boundary conditions, International Journal of Solid and Structures, Vol. 45 (2008), pp. 5322-5336.